SUPPLEMENTARY FIGURE LEGENDS

Figure S1. Schematic of Target RNA in the Presence or Absence of Anti-tag, Related to Figure 1.

(A) Secondary structure diagram of crRNA repeat region in *Leptotrichia shahii* (LshCas13a), *Leptotrichia buccalis* Cas13a (LbuCas13a), *Listeria seeligeri* Cas13a (LseCas13a), and *Lachnospiraceae bacterium* Cas13a (LbaCas13a) systems. 8-nt tag region at 3'-end including bulge and 3'-flank are highlighted with blue background.

(B, C) Secondary structure diagram of crRNA and target RNA used for structural studies and *in vitro* enzymatic assay monitoring cleavage of non-target substrate RNA by LshCas13a (B) and LbuCas13a (C) in the presence or absence of anti-tag. The crRNA tag region is highlighted with blue background. RNA6 is used for structure determination of LshCas13a. Nucleotides not observed in the structures are indicated by dashed box.

(D, E) Plasmids interference activities in *E. coli* cells harboring *LshCas13a* (panel D) or *LbuCas13a* (panel E) plasmids as well as a tet-induced EYFP plasmid. The transcription of EYFP mRNA was induced by adding tetracycline. Ten-fold serial dilution of cells as indicated were spotted onto double-antibiotic plates.

(F) Secondary structure diagram of LbuCas13a crRNA and target RNA with 21-nt spacer and target segment in the presence or absence of anti-tag. The crRNA tag region is highlighted with blue background.

(G) Elution profiles run from a Superdex 200 10/300 GL size exclusion column of LbuCas13a in complex with target RNA in the presence or absence of anti-tag, with a shortened 21-nt spacer. The sequence and secondary structure of crRNA and target RNAs are shown in Figure S1D. Anti-tag has no effect on the assembly of LbuCas13a-crRNA-target RNA ternary complex, but changes the conformation of the ternary complex into an inactive state.

Figure S2. Cryo-EM Reconstruction of LshCas13a-crRNA-Target RNA Complex with 8-nt Anti-tag, Related to Figure 2.

(A) Representative cryo-EM micrograph.

(B) Representative 2D class averages calculated by Relion.
(C) Overview of image processing and refinement strategy.
(D) Euler angle distribution showing the relative orientation of the particles used in the final 3D reconstruction.
(E) Fourier Shell Correlation (FSC) curve between two semi-independently refined halves of the data (blue curve), and between the cryo-EM map and corresponding refined model (red curve).
(F) Final 3D reconstruction map colored by local resolution.

Figure S3. Density Map to the Structure Models for LshCas13a-crRNA-Target RNA Complex with 8-nt Anti-tag, Related to Figure 2, 3, 4, 5 and 6.

(A) Electron density maps and fits for HEPN, Helical, and Linker domains of LshCas13a in the complex. There is no clear density map for the NTD domain.
(B) Electron density maps and fits for guide and target RNAs including tag:anti-tag segment in the complex.

Figure S4. Conformational Changes LbuCas13a Upon Target RNA Loading, Related to Figures 5 and 6.

(A) Structural comparison between LbuCas13a-crRNA binary complex and LbuCas13a-crRNA-target RNA ternary complex. Vector lengths correlate with the domain motion scales. Arrows show the directions of domain movement from pre-target-bound to target-bound states.
(B) Structural comparison of the NTD, Helical-I, HEPN-I, HEPN-II, Linker and Helical-II domains between LbuCas13a-crRNA binary (in silver) and LbuCas13a-crRNA-target RNA ternary (in color) complexes. Arrows indicate the domain movements. The key catalytic residues of HEPN domains are indicated by red (pre-target-bound binary) and black (target-bound ternary) asterisks, respectively.
(C) Binding with target RNA widens the guide:target duplex-binding channel in the LbuCas13a-crRNA-target RNA ternary complex.

(D, E) Architectures of crRNA in LbuCas13a-crRNA-target RNA ternary complex (panel D). The details of tag region are showing in the panel E, with target bound crRNA in color and pre-target-bound crRNA in silver.
(F) The tag region of crRNA in LbuCas13a-crRNA-target RNA ternary complex makes interactions with Cas13a.
(G, H) Recognition of Lbu-crRNA tag region by LbuCas13a in pre-target-bound and Target-bound States, Related to Figure 6 and 7. Hydrophilic interactions between Lbu-crRNA tag region and LbuCas13a in LbuCas13a-crRNA binary (panel G) and LbuCas13a-crRNA-target RNA ternary (panel H) complexes.

Figure S5. Cryo-EM Reconstruction of LshCas13a-crRNA-Target RNA Complex without Anti-tag, Related to Figures 5 and 6.
(A) Representative cryo-EM micrograph. LshCas13a and dissociated RNA are indicated by red and blue circles, respectively.
(B) Representative 2D class averages calculated by Relion. Potential 2D classes of LshCas13a-crRNA-target RNA ternary complex are indicated by blue boxes.
(C) Overview of image processing and refinement strategy.
(D) Euler angle distribution showing the relative orientation of the particles used in the final 3D reconstruction.
(E) Final 3D reconstruction map of LshCas13a-crRNA-target RNA ternary complex. The direction of preferred orientation is indicated by the black arrow.

Figure S6. Sequence Alignment of Cas13a, Related to Figure 6.
Sequence alignment of LshCas13a and LbuCas13a. The secondary structures of LshCas13a and LbuCas13a are shown on top and bottom, respectively. Identical residues are written with white bold character and boxed in red, while similar residues are written with black bold character and boxed in yellow. The HEPN-I domain is further separated into two subdomains HEPN-I-1 and HEPN-I-2 by Helical-II domain (see domain organization in Figure 2A). HEPN-I-1 and HEPN-II domains are highlighted by green and salmon box, respectively. The HEPN-I-2 in LshCas13a and LbuCas13a domains are highlighted by regular box and dashed

box, respectively. The key catalytic residues are indicated by black triangle, while mutations investigated in this study are indicated by blue triangle.

Figure S7. Structural Comparison of Cas13a crRNA repeat segment, Related to Figure 6.

Structural comparison of the crRNA repeat region between LshCas13a-crRNA binary (in violet) and LbuCas13a-crRNA binary (in gray) complexes, with the details of tag region shown in the zoom-in panel.

Table S1. Summary of cryo-EM data collection and model refinement for LshCas13a-crRNA-target RNA complex with 8-nt anti-tag.

Related to Figure 2 and S2.

Data collection and processing	
Magnification	29,000
Voltage (kV)	300
Electron exposure (e^-/ Å^2)	48
Defocus range (mm)	-1.0 to -2.2
Pixel size (Å)	0.86
Initial particles (no.)	829,249
Final particles (no.)	212,861
Map resolution (Å)	3.06
FSC threshold	0.143
Map sharpening B factor (Å2)	-89.0
Refinement	
Model resolution (Å)	3.31
FSC threshold	0.5
Model composition	
Protein residues	979
Nohydrogen atoms	9,451
B factors (Å^2)	
RMS deviations	
Bond lengths (Å)	0.005
Bond angles (°)	0.949
Validation	
MolProbity score	1.70
Clashcore	3.70
Poor rotamer (%)	0.62
Ramachandran plot (%)	
Favored	90.23
Allowed	9.77
Outliers	0

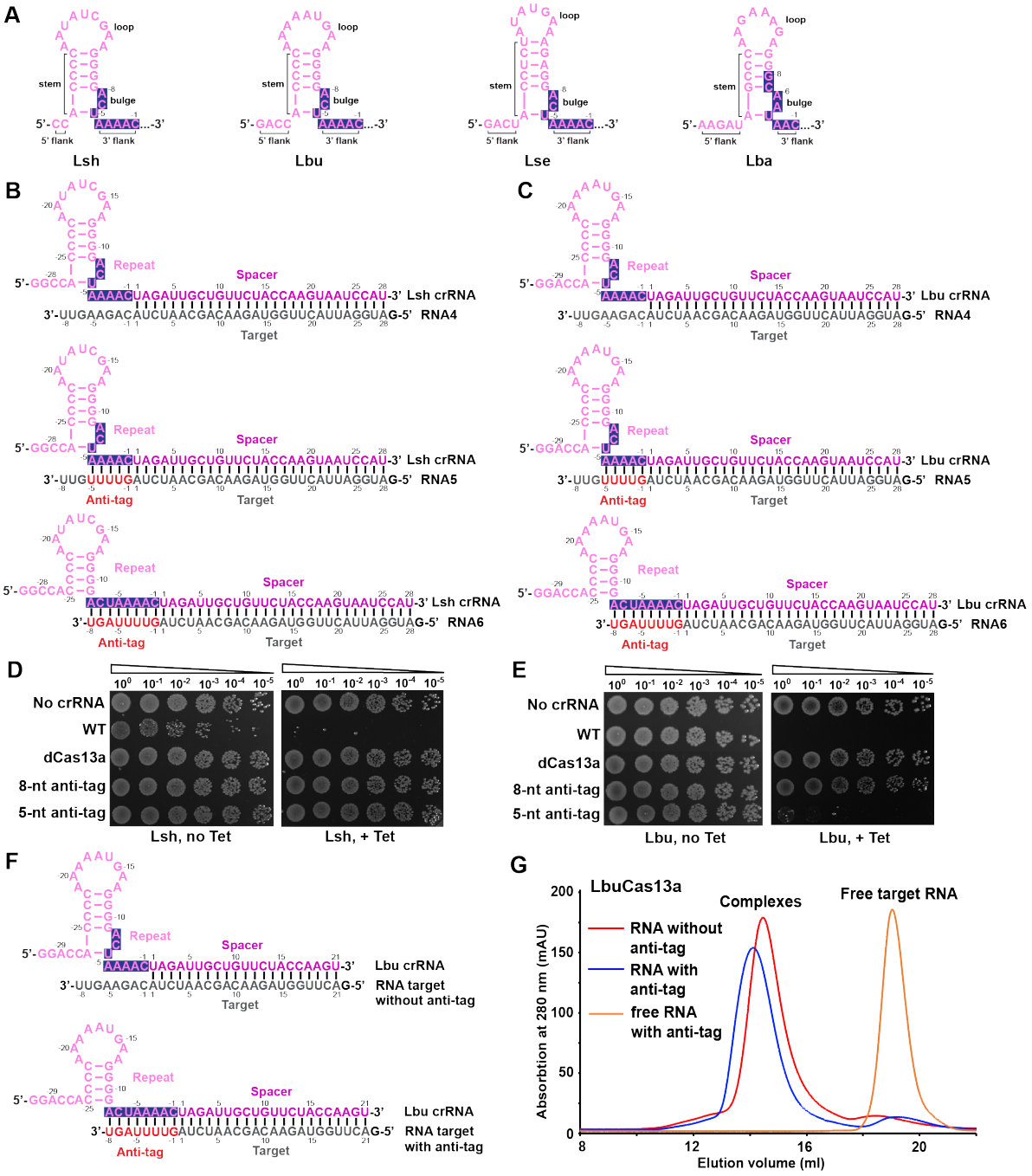
A
loop
stem
bulge
5'-CC
AAAAC...-3'
5' flank
3' flank
Lsh
5'-GACC
Lbu
5'-GACU
Lse
5'-AAGAU
AAC...-3'
Lba
B
Repeat
Spacer
5'-GGCCA
AAAACUAGAUUGCUGUUCUACCAAGUAAUCCAU-3' Lsh crRNA
3'-UUGAAGACAUCUAACGACAAGAUGGUUCAUUAGGUAG-5' RNA4
Target
AAAACUAGAUUGCUGUUCUACCAAGUAAUCCAU-3' Lbu crRNA
3'-UUGAAGACAUCUAACGACAAGAUGGUUCAUUAGGUAG-5' RNA4
Target
Anti-tag
3'-UUGUUUUGAUCUAACGACAAGAUGGUUCAUUAGGUAG-5' RNA5
Target
5'-GGCCAC
ACUAAAACUAGAUUGCUGUUCUACCAAGUAAUCCAU-3' Lsh crRNA
3'-UGAUUUUGAUCUAACGACAAGAUGGUUCAUUAGGUAG-5' RNA6
Target
ACUAAAACUAGAUUGCUGUUCUACCAAGUAAUCCAU-3' Lbu crRNA
3'-UGAUUUUGAUCUAACGACAAGAUGGUUCAUUAGGUAG-5' RNA6
Target
D
No crRNA
WT
dCas13a
8-nt anti-tag
5-nt anti-tag
Lsh, no Tet
Lsh, + Tet
E
Lbu, no Tet
Lbu, + Tet
F
5'-GGACCA
AAAACUAGAUUGCUGUUCUACCAAGU-3'
Lbu crRNA
3'-UUGAAGACAUCUAACGACAAGAUGGUUCAG-5'
RNA target without anti-tag
Target
5'-GGACCAC
ACUAAAACUAGAUUGCUGUUCUACCAAGU-3'
Lbu crRNA
3'-UGAUUUUGAUCUAACGACAAGAUGGUUCAG-5'
RNA target with anti-tag
Anti-tag
Target
G
LbuCas13a
Complexes
Free target RNA
RNA without anti-tag
RNA with anti-tag
free RNA with anti-tag
Absorbtion at 280 nm (mAU)
Elution volume (ml)

Figure S1

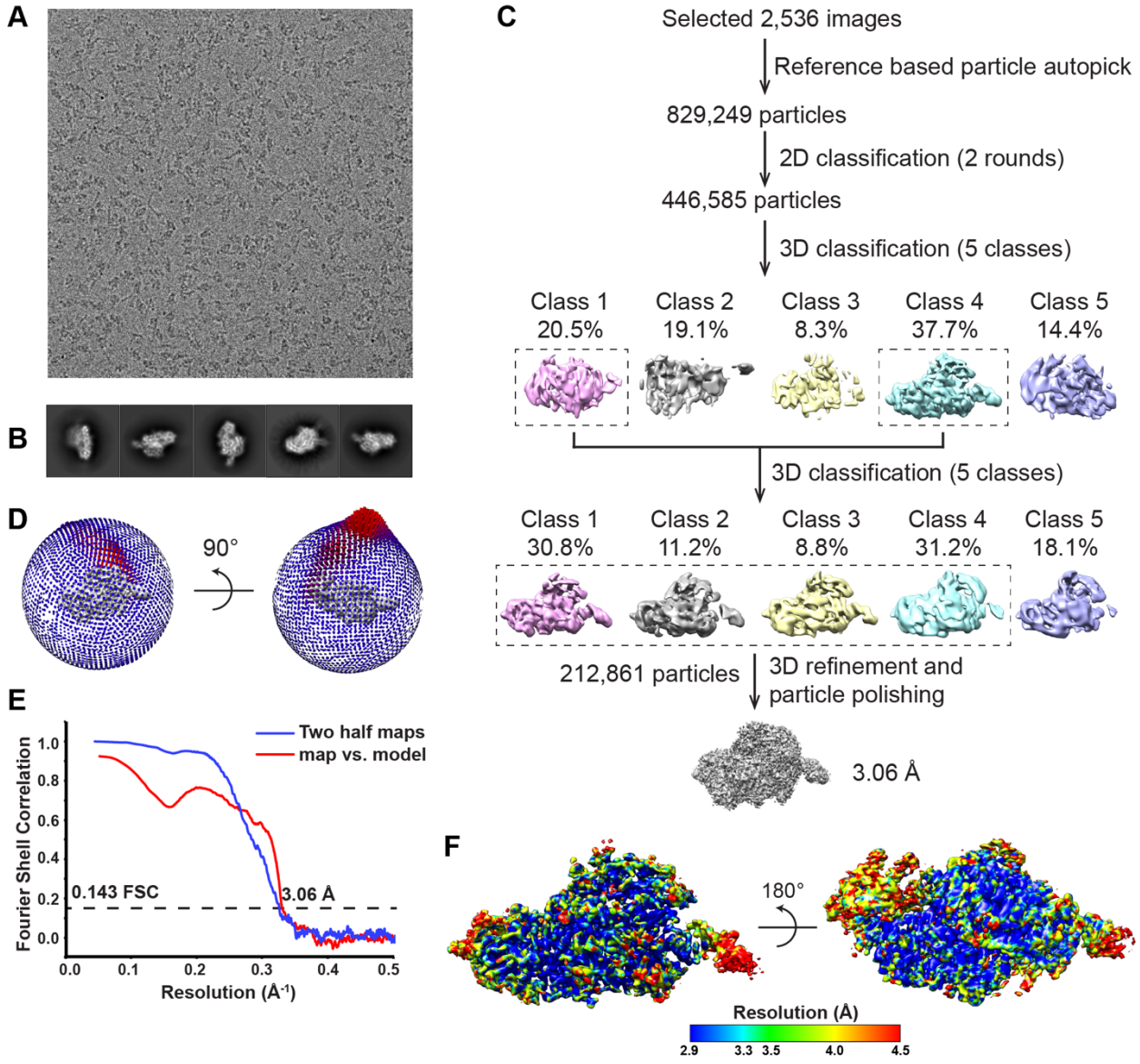
A
B
C
Selected 2,536 images
Reference based particle autopick
829,249 particles
2D classification (2 rounds)
446,585 particles
3D classification (5 classes)
Class 1
20.5%
Class 2
19.1%
Class 3
8.3%
Class 4
37.7%
Class 5
14.4%
3D classification (5 classes)
Class 1
30.8%
Class 2
11.2%
Class 3
8.8%
Class 4
31.2%
Class 5
18.1%
212,861 particles
3D refinement and
particle polishing
3.06 Å
D
90°
E
Two half maps
map vs. model
Fourier Shell Correlation
0.143 FSC
3.06 Å
Resolution (Å-1)
F
180°
Resolution (Å)
2.9
3.3
3.5
4.0
4.5

Figure S2

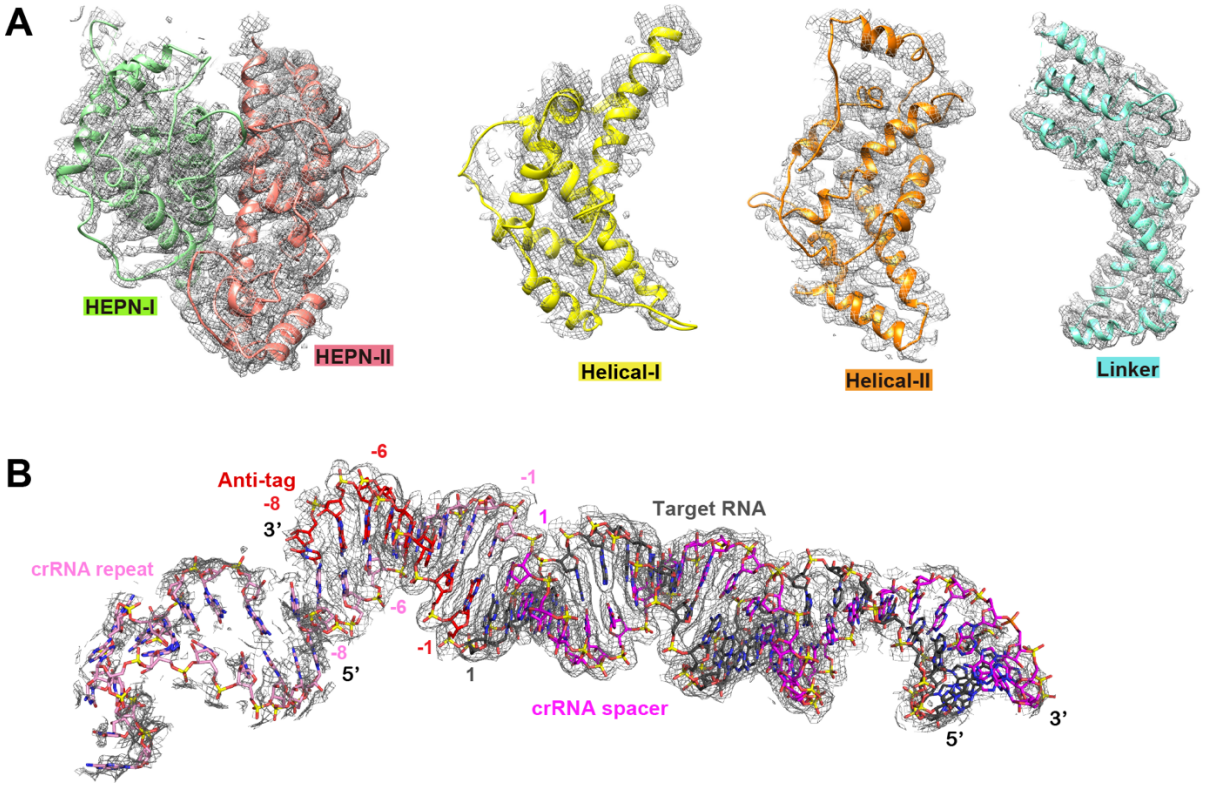
A
HEPN-I
HEPN-II
Helical-I
Helical-II
Linker
B
Anti-tag
-8
3'
-6
-1
1
Target RNA
crRNA repeat
-6
-8
5'
-1
1
crRNA spacer
5'
3'

Figure S3

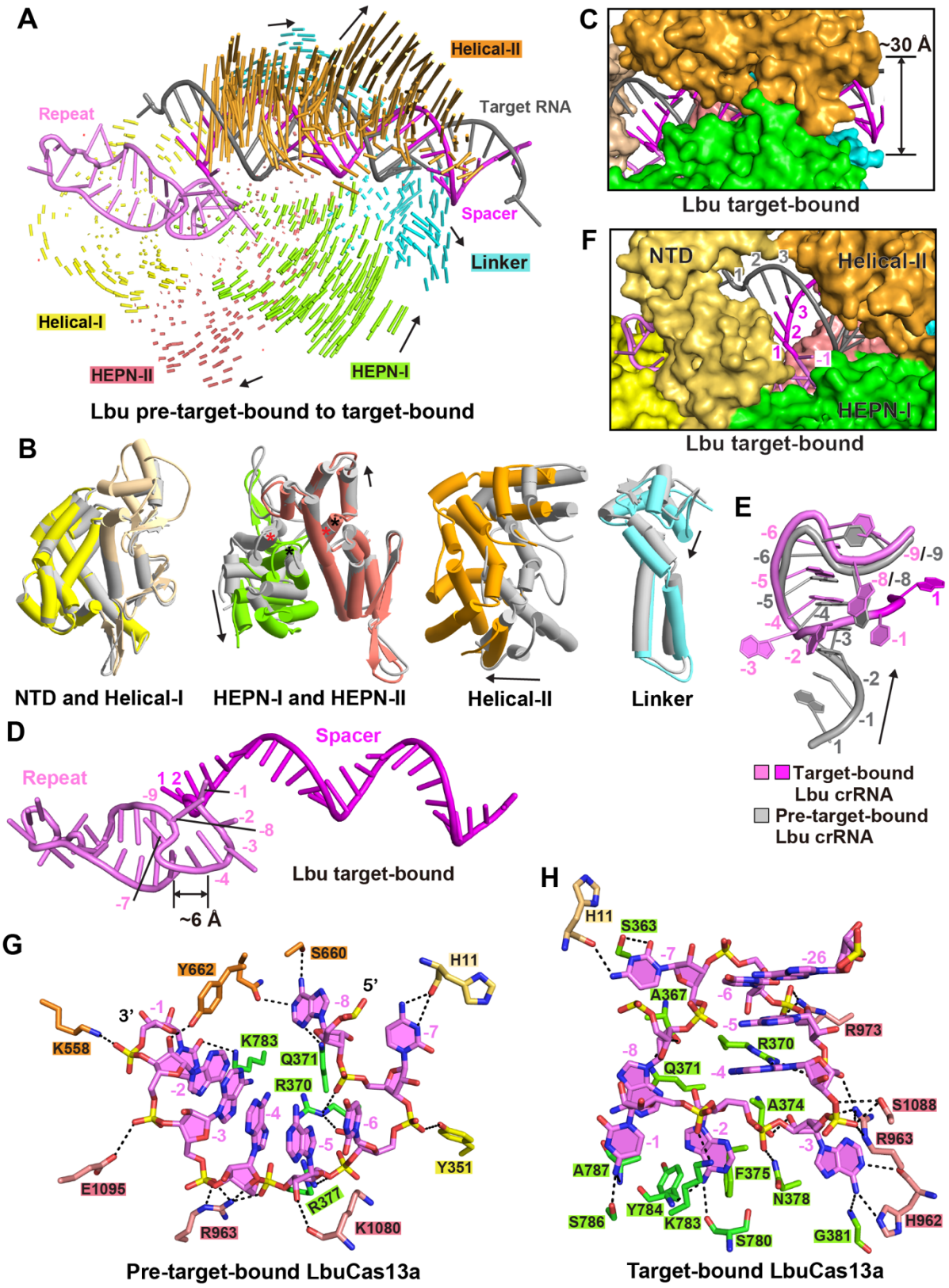
A
Helical-II
Target RNA
Repeat
Spacer
Linker
Helical-I
HEPN-II
HEPN-I
Lbu pre-target-bound to target-bound
C
~30 Å
Lbu target-bound
F
NTD
Helical-II
HEPN-I
Lbu target-bound
B
NTD and Helical-I
HEPN-I and HEPN-II
Helical-II
Linker
E
Target-bound Lbu crRNA
Pre-target-bound Lbu crRNA
D
Spacer
Repeat
~6 Å
Lbu target-bound
G
Y662
S660
H11
5'
3'
K558
K783
Q371
R370
E1095
R963
R377
K1080
Y351
Pre-target-bound LbuCas13a
H
H11
S363
A367
R973
R370
Q371
A374
S1088
R963
A787
F375
N378
S786
Y784
K783
S780
G381
H962
Target-bound LbuCas13a

Figure S4

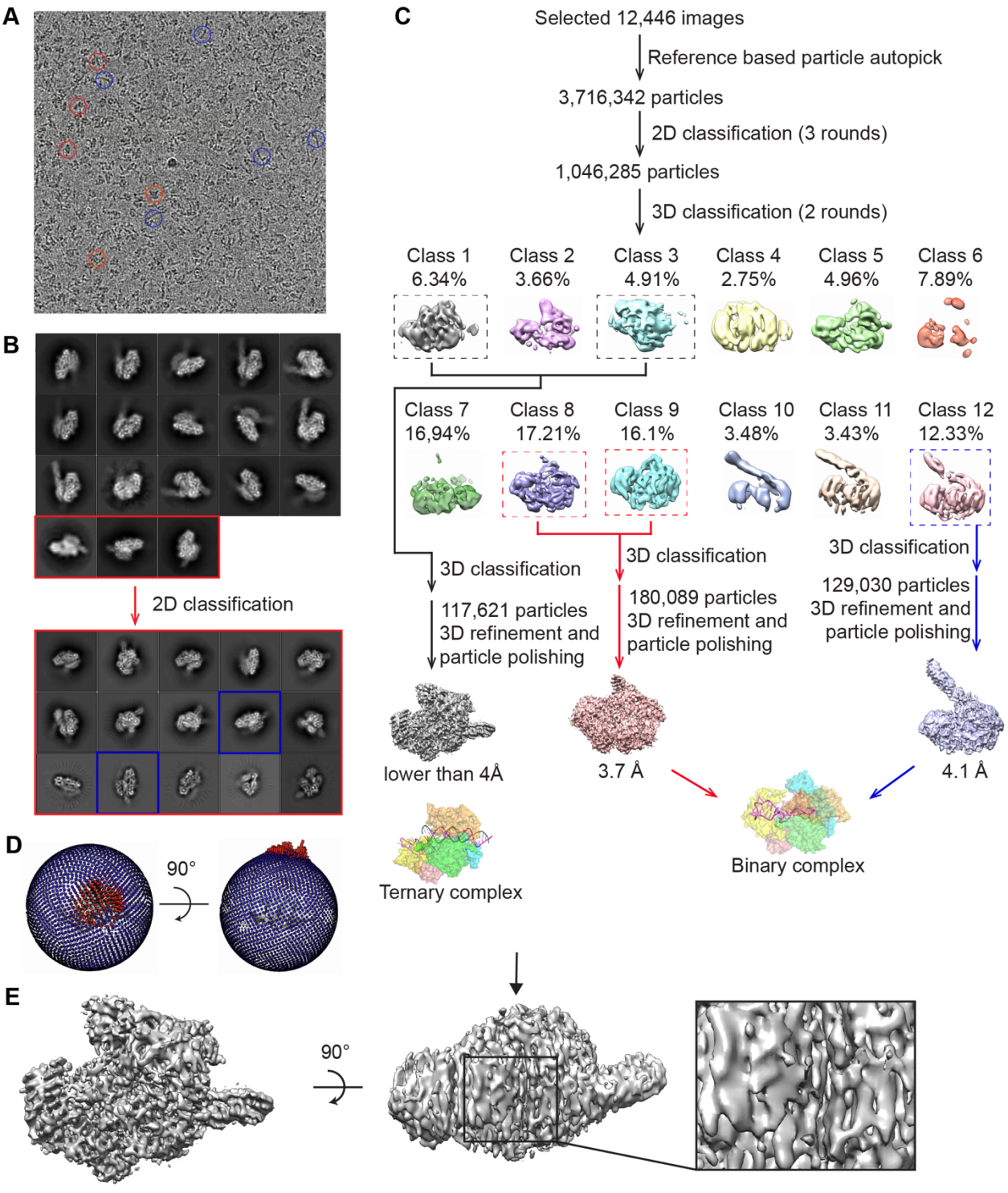
A
B
2D classification
C
Selected 12,446 images
Reference based particle autopick
3,716,342 particles
2D classification (3 rounds)
1,046,285 particles
3D classification (2 rounds)
Class 1
6.34%
Class 2
3.66%
Class 3
4.91%
Class 4
2.75%
Class 5
4.96%
Class 6
7.89%
Class 7
16,94%
Class 8
17.21%
Class 9
16.1%
Class 10
3.48%
Class 11
3.43%
Class 12
12.33%
3D classification
117,621 particles
3D refinement and
particle polishing
3D classification
180,089 particles
3D refinement and
particle polishing
3D classification
129,030 particles
3D refinement and
particle polishing
lower than 4Å
3.7 Å
4.1 Å
Ternary complex
Binary complex
D
90°
E
90°

Figure S5

Figure S6

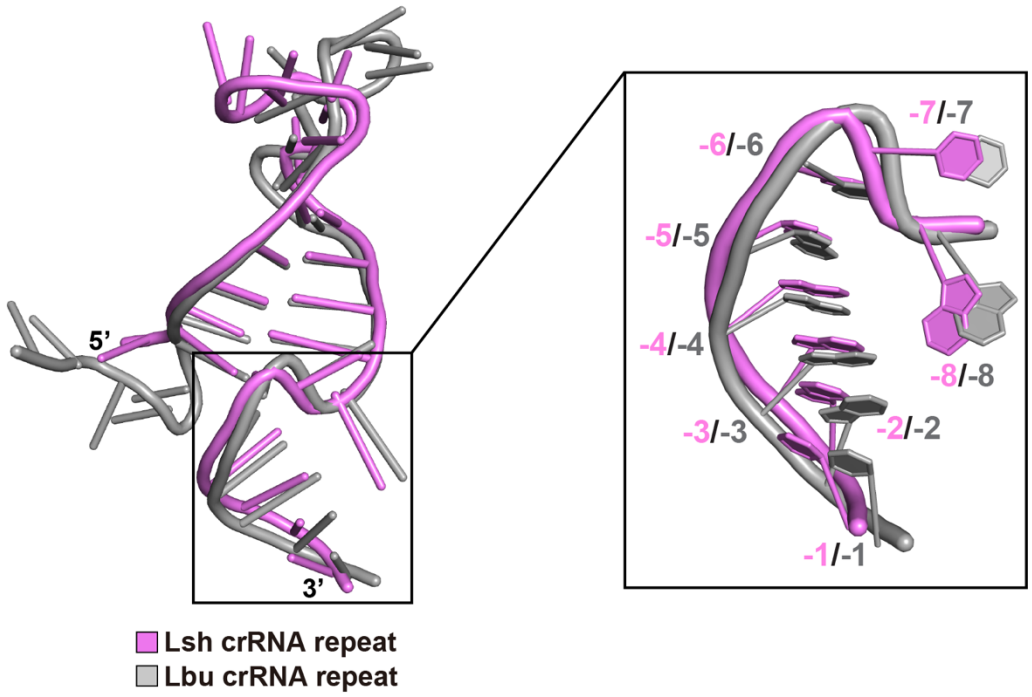

Figure S7